



Study of fluid flow in grooved micro and nano-channels via dissipative particle dynamic: a tool for desalination membrane design

Dorothea Kasiteropoulou*, Theodoros Karakasidis, Antonios Liakopoulos

Laboratory of Hydromechanics and Environmental Engineering, School of Engineering, University of Thessaly, 38334 Volos, Greece, Tel. +30 24210 74329; Fax: +30 24210 74169; email: dkasiter@uth.gr (D. Kasiteropoulou), Tel. +30 24210 74163; Fax: +30 24210 74169; email: thkarak@uth.gr (T. Karakasidis), Tel. +30 24210 74111; Fax: +30 24210 74169; email: aliakop@uth.gr (A. Liakopoulos)

Received 16 March 2015; Accepted 7 January 2016

ABSTRACT

A number of recent studies strongly suggest that nanostructured materials, such as carbon nanotubes, nanoporous graphene, and zeolites, can form the basis for the fabrication of next generation membranes for reverse osmosis desalination. In the present work, we investigate the influence of the wall roughness and external driving force on the flow pattern and energy losses in nano and microchannel flow through the estimation of the effective velocity slip at solid walls and other macroscopic quantities such as density, velocity, and pressure. The investigation is based on the dissipative particle dynamics simulation method and the flow studies concern flows between parallel plates with the protrusions located at the upper wall. Roughness is modeled by periodically spaced rectangular protruding elements. When compared to the smooth channel case, lower flow velocities are observed in the central part of the channel for all cases studied. This reduction of velocities becomes more pronounced as the protrusion height increases. For the microchannel, density, pressure, and temperature remain almost constant in the central part of the channel and their pattern near and inside the cavities depends on the protrusion shape. The results show that the slip velocity, both for the nano and microchannel flow, is reduced as the protrusion length is reduced and the protrusion height is increased for both the upper rough and the lower flat wall. As far as the external driving force is concerned, it seems that the slip velocity increases as the external driving force increases for constant protrusion size. The study of these parameters is of particular importance for the design of filters and membranes based on nanomaterials employed in the desalination process as well as contaminant removal from water.

Keywords: Grooved microchannels; Nanochannels; Slip velocity; Dissipative particle dynamics; Protrusion size effect; Desalination

*Corresponding author.

Presented at the 12th International Conference on Protection and Restoration of the Environment (PRE XII) 29 June—3 July 2014, Skiathos Island, Greece

1. Introduction

Current desalination installations are characterized by large energy requirements and high cost [1]. A number of recent studies strongly suggest that nanostructured materials such as carbon nanotubes (CNT), nanoporous graphene (NPG), and zeolites can form the basis for the fabrication of next generation membranes for reverse osmosis desalination [1,2]. These membranes are able to function as molecular sieves rejecting salt ions, while allowing water molecules to pass through the pores thus achieving high permeabilities, compared to membranes currently in use, these membranes offer the possibility of increased efficiency and capacity in the next generation desalination systems.

The study of flow in tubes and channels at the micro and nanoscale is required in order to understand the fluid dynamical aspects of the membrane function and estimate the pressure differentials required for the fluid motion through the membrane pores.

Experiments cannot deliver all answers at the micro and nanoscale channels due to the very small length and time scales involved and due to sophisticated and expensive equipment that are required. On the other hand, numerical simulation methods are especially important at these scales for fundamental understanding and technical design.

The density, velocity, velocity slip, temperature, and pressure effect has been studied by several authors theoretically in an attempt to highlight the main issues related to this diverse complex phenomenon and its implications. Slip at solid walls can potentially lead to great reduction of the required flow driving force and to flow instabilities, such as shark-skin formation and spurt flow. Hence, slip complicates the analysis of fluid systems and introduces serious practical difficulties [3]. Niavarani and Priezjev [4] investigated the combined effect of surface roughness and shear rate on slip flow of simple fluids by molecular dynamics simulation and found that in the region where the curved boundary faces the mainstream flow, the local slip is suppressed due to the increase in pressure. Sun et al. [5] investigated the effects of surface wettability and topology in the multi-scale liquid flow in micro/nanochannels. Analysis on the flow friction shows that the pressure gradient decreases following a power law with increasing channel height. The confinement on the liquid molecules will equivalently narrow the channel, where larger pressure gradient is needed to keep the flow conditions from changing. The larger the roughness is, the more obvious the influence will be. When the channel height

becomes larger, both slip velocity and relative slip length will gradually converge to zero, which means that different flow boundaries will be unified to be nonslip at conventional spatial scale. Priezjev [6] reported the results obtained from molecular dynamic simulations of the friction at an interface between polymer melts and weakly attractive crystalline surfaces. He found that the friction coefficient at small slip velocities exhibits a distinct maximum which appears due to shear-induced alignment of semiflexible chain segments in contact with solid walls and at large slip velocities, the friction coefficient is independent of the chain stiffness. Later, Chen et al. [7] estimated the velocity slip on curved surfaces in a Couette flow studied by molecular dynamics simulation. They found that the slip length as conventionally measured at a flat wall in Couette flow is the same as that for all other cases with curved and rotating boundaries, provided that the atomic interactions are the same and boundary shape is properly taken into account.

In the case of dissipative particle dynamics simulation method, boundary conditions play a significant role in the slip length performance. The Maxwellian and bounce back [8–10] boundary conditions lead in fluctuations near the wall in the velocity profile and thus significant slip length. Kasiteropoulou et al. [11,12] investigated the flow in periodically grooved nano and microchannels by the dissipative particle dynamics simulation method. They observed that the slip velocity at the rough wall is reduced systematically as the protrusion length is reduced and as the protrusion height increases. They also found that the slip velocity at the flat wall depends on the protrusion size even for small protrusion heights (10% of the channel width). Yang [13] investigated the surface roughness effect on the nanorheology and fluid slip of simple fluids in hydrophobic and hydrophilic nanochannels and found that no-slip or negative slip is observed at the interface due to the increase in drag resistance. Jabbarzadeh et al. [14] investigated the effect of wall roughness characteristics and the molecular length of the lubricating fluid in a flow of liquid hexadecane in sinusoidal wall channels and found that larger roughness amplitudes result in a decrease in the slip and also that with shorter molecules, the amount of slip is dramatically lower.

The velocity slip can affect transport phenomena. A study is presented in Amhalhel and Furmański [15], who investigated problems of modeling flow and heat transfer in porous media. The applications could be summarized in the following [15]: (a) Agricultural applications (e.g. fermentation process in food industries, freeze-drying of food products, grain storage,

soil heating to increase the growing season), (b) Environmental applications (e.g. groundwater pollution, groundwater systems, storage of radioactive waste, water movement in geothermal reservoirs), (c) Industrial applications (e.g. artificial freezing of ground as a structural support and as a water barrier for construction and mining purposes, crude oil production and recovery systems, porous radiant burners, post-accident heat removal, solidification of castings, study of heat transfer phenomenon of buried electrical cables and transformer cables, fluidized bed combustion), (d) Thermal conversion and storage systems (e.g. catalytic reactors, geothermal systems, packed beds, fluidized bed, heat pipes, sensible, latent, and thermochemical energy storage systems).

More specifically, nanomaterials such as CNT have been proposed for advanced treatment of wastewater and desalination [16]. The effect of the liquid/vapor interfaces in the transport of water across osmosis membranes comprising short hydrophobic nanopores that separate two fluid reservoirs has been investigated [17]. It was shown experimentally that mass transport is limited by molecular reflection from the liquid/vapor interface below a certain length scale, which depends on the transmission probability of water molecules across the nanopores and on the condensation probability of a water molecule incident on the liquid surface. Molecular dynamics of NPG membranes [18] indicate that they can reject salt ions while letting water flow at permeabilities several orders of magnitude higher than existing membranes. The results show that the hydrophobic character of surfaces affects water flow. Such tools can contribute greatly to a better design of desalination membrane materials but also water purification systems.

The present work focuses on the investigation of roughness effects in planar nanochannels and micro-scale channels with a mesoscopic method. The influence of model parameters on density, velocity, slip velocity, and pressure in the rough and the flat wall of the channel, is studied. This paper is set up as follows. In Section 2, the simulation method is presented. Results are shown and discussed in Section 3, while Section 4 contains concluding remarks.

2. Simulation method

2.1. Channel geometry

We study the flow between two stationary parallel solid plates (see Fig. 1). The lower wall is flat, while the upper wall is rough characterized by periodically placed rectangular protruding elements. We considered roughness of three different lengths: $l_{r1} = 0.5 l_{tot}$

$l_{r2} = 0.25 l_{tot}$, $l_{r3} = 0.125 l_{tot}$ (for the nanochannel case) and $l_{r3} = 0.167 l_{tot}$ (for the microchannel case) (case $l_{r1} = 0.5 l_{tot}$ corresponds to one rectangular groove in the computational domain, $l_{r2} = 0.25 l_{tot}$ to two rectangular grooves and $l_{r3} = 0.125 l_{tot}$ to three rectangular grooves for the microchannel and four for the nanochannel case) and four different heights [$h_1 = 0.10 H$ ($0.125 \bar{h}$), $h_2 = 0.20 H$ ($0.250 \bar{h}$), $h_3 = 0.30 H$ ($0.375 \bar{h}$), $h_4 = 0.40 H$ ($0.50 \bar{h}$), where H represents the height of the computational domain along the y -direction and \bar{h} the distance between the two parallel solid plates]. Baseline dimensions of all computational domains in x -, y - and z -directions are $L_x \times L_y \times L_z = 1.11 \mu\text{m} \times 1.3 \mu\text{m} \times 1.1 \mu\text{m}$ for the micro and $3.77 \text{ nm} \times 4.72 \text{ nm} \times 3.77 \text{ nm}$ for the nanochannel (in dissipative particle dynamics (DPD) units, the dimensions are $L_x \times L_y \times L_z = 11.14 r_c \times 13.00 r_c \times 11.14 r_c$ and $11.09 r_c \times 13.87 r_c \times 11.09 r_c$, respectively, r_c being the cut-off distance of the interactions between particles). Conversion from DPD units to physical units is discussed in detail in Kumaretal. [9].

2.2. Mathematical model and computational details

The DPD system consists of N particles. For the i -th particle, we denote mass by m_i , position by r_i , and velocity by v_i , $i = 1, 2, \dots, N$. For a single-component DPD liquid, the forces exerted on a particle i due to particle j consists of three terms: (1) the conservative force F_{ij}^C , (2) the dissipative force F_{ij}^D , and (3) a random force F_{ij}^R , given by,

$$F_{ij}^C(r_{ij}) = \begin{cases} \alpha_{ij}(1 - r_{ij}/r_c)\hat{r}_{ij}, & \text{for } r_{ij} \leq r_c \\ 0, & \text{for } r_{ij} > r_c \end{cases} \quad (1)$$

$$F_{ij}^D = -\gamma\omega^D(r_{ij})(v_{ij} \cdot \hat{r}_{ij})\hat{r}_{ij} \quad (2)$$

$$F_{ij}^R = \sigma\omega^R(r_{ij})\xi_{ij}\hat{r}_{ij} \quad (3)$$

where $r_{ij} = r_i - r_j$, $r_{ij} = |r_{ij}|$, $\hat{r}_{ij} = \frac{r_{ij}}{|r_{ij}|}$, $v_{ij} = v_i - v_j$ [19] and α_{ij} is the maximum repulsion between particles i and j [20]. The coefficients γ and σ determine the amplitude of the dissipative and random forces, respectively, while ω^D and ω^R are appropriate weight functions [19]. The weight functions ω^D and ω^R provide the range of interaction for the dissipative and random forces [20]. In Eq. (3), ξ_{ij} is a random variable with Gaussian statistics [21,22]. By enforcing $\xi_{ij} = \xi_{ji}$, one satisfies the principle of momentum conservation [23]. All the forces between particle i and j vanish beyond a cut-off radius r_c [23]. The random force coefficient, σ , the system temperature, and the simulation timestep is the same for all cases studied here and

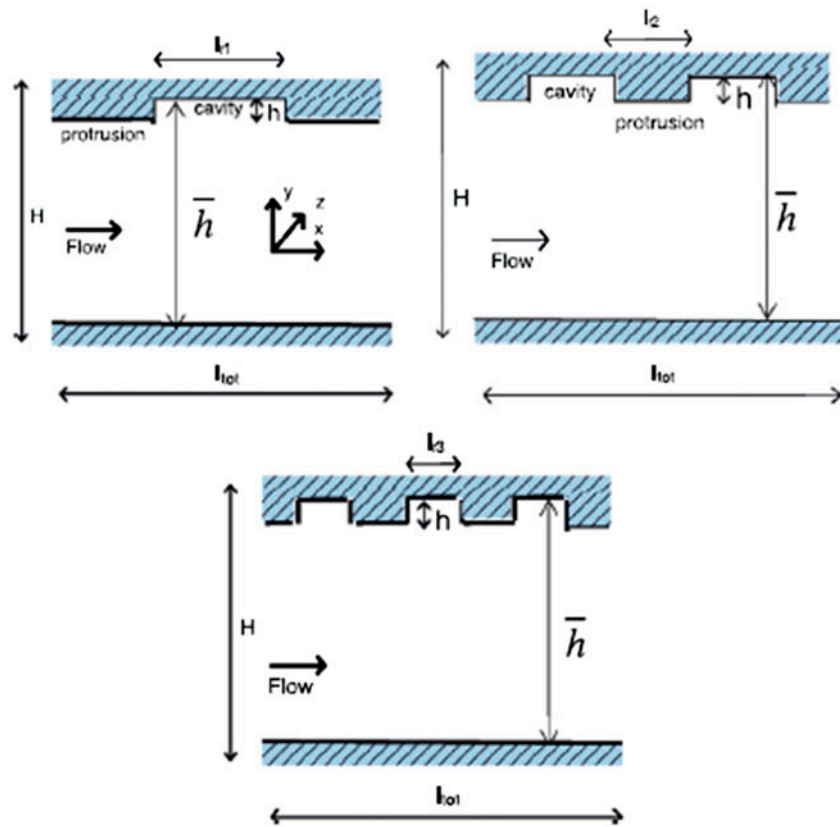


Fig. 1. Schematics of channel geometry and protrusion/cavity shapes.

their value was chosen following the methodology proposed by Groot and Warren [21].

The requirement of canonical distribution sets two conditions linking the random and dissipative forces. The first one couples the weight functions through:

$$\omega^D(r_{ij}) = [\omega^R(r_{ij})]^2 \quad (4)$$

and the second one couples the strengths of the random and dissipative forces via.

$$\sigma^2 = 2\gamma k_B T \quad (5)$$

where k_B is the Boltzmann constant [25]. The typical choice for the weight functions is:

$$\omega^R(r_{ij}) = \begin{cases} (1 - r_{ij}/r_c)^p, & \text{for } r_{ij} \leq r_c \\ 0, & \text{for } r_{ij} > r_c \end{cases} \quad (6)$$

where $p = 1$, for the standard DPD method [19].

The time evolution of velocities and positions of particles are described by the following equations [8]:

$$dr_i = v_i dt \quad (7)$$

$$dv_i = \frac{1}{m} (F_i^C dt + F_i^D dt + F_i^R \sqrt{dt}) \quad (8)$$

where $F_i^C = \sum_{i \neq j} F_{ij}^C$, and $F_i^R = \sum_{i \neq j} F_{ij}^R$.

All simulations are conducted using the open-source LAMMPS package [24]. The number density of the DPD fluid, n_f , is set equal to 3 for the nanochannel case and 10 for the microchannel, while the random and dissipative force, parameters, σ and γ , respectively, are set equal to those described in Pivkin and Karniadakis [8]. System temperature is kept constant at $T^* = 1$ (in real units, the system temperature is equal to 300 K). The value of parameter a_{ij} has been selected so that the dimensionless compressibility of the simulated DPD fluid corresponds to a typical liquid, such as water (for the calculation of compressibility, see [25]). This value of a_{ij} is employed in all types of interactions: fluid–fluid, wall–wall, and wall–fluid. We

remind the reader that the cross interaction term obeys the relation $a_{wf} = (a_{ww} a_{ff})^{1/2}$ (see for example Pivkin and Karniadakis [8]). The type of the surface (hydrophilic or hydrophobic) is controlled via the fluid–wall interaction through the conservative force parameter a_{ij} (Eq. (1)), specifically by choosing appropriately the ratio of the a_{ij} parameters for the fluid–wall interaction vs. a_{ij} parameters for fluid–fluid interactions [26].

In this work, we employed $a_{ff} = 25$ and $a_{wf} = 25$ with $r_c = 1.0 \sigma$ for the cut-off radius for particle interactions and $N_m = 1$ (one atom per DPD particle—nanochannel case). We examined the effect of the magnitude of the externally applied force by assigning four values ($F_{ext} = 0.01, 0.02, 0.03, 0.04$ DPD units). The external driving force is applied on each particle along the x -direction to drive the flow. We then changed the number of atoms per DPD particle equal to $N_m = 2.5 \times 10^6$ (microchannel case) atoms per particle, along with the particle interactions coefficient: $a_{ff} = a_{wf} = a_{ww} = 7.5$ and $r_c = 1.0 \sigma$.

Periodic boundary conditions are employed along x - and z -directions. Appropriate boundary conditions need to be enforced in order to avoid that fluid particles penetrate the wall, since the effective forces are not sufficient to prevent wall penetration. In the present study, we have chosen to employ the bounce back conditions, in which both components of the velocity are reversed [10]. Wall particles are bound on sites of a cubic lattice and their velocities are set equal to zero. The simulation timestep is $\Delta t = 0.01 \sqrt{mr_c^2/k_B T}$ (0.015 ps for the nanochannel and $7.6 \times 10^{-3} \mu s$ for the microchannel in physical units). The duration of each simulation is 5×10^5 time steps. Pressure, number density, temperature, and streaming velocity bin values are averaged over the last 2.5×10^5 time steps of the simulation.

2.3. Macroscopic property evaluations

Local macroscopic property values are calculated in parallelepiped bins. Results presented in this work are obtained by dividing the computational domain into $4 \times 80 \times 80, 8 \times 80 \times 80, 16 \times 80 \times 80$ bins along the direction x, y, z , respectively, for post processing. To extract average profiles (for pressure, density, velocity, temperature), mean values over space are computed at each layer along the channel for each time step, and these values are then averaged over time. For the calculation of the slip velocity, $1 \times 80 \times 80$ bins were employed. Global velocity profile fit used in Couette (linear) or Poiseuille (parabolic) flow studies cannot be employed here because of the presence of the upper wall protrusions (an example of slip velocity profile is

presented in Fig. 2). For this reason, a local estimation procedure of the slip velocity was performed. The slip velocity in the lower wall is estimated by linear extrapolation on the basis of the first and second (nano), second and third (micro) non-zero fluid velocity values closest to the flat wall. The average slip velocity at the upper rough wall is obtained by local estimation at the $y = \text{const.}$ middle plane of the protrusion.

Pressure values are obtained from the trace of the stress tensor:

$$p = -\frac{1}{3} \text{tr} S \tag{9}$$

where the stress tensor, S , is calculated using the Irving–Kirkwood theory [28,29]:

$$S = -\frac{1}{V} \left[m \sum_i (v_i - v)(v_i - v) + \frac{1}{2} \sum_i \sum_{j \neq i} r_{ij} F_{ij} \right] \tag{10}$$

where V is the volume of the computational bin, v is the corresponding stream velocity, and F_{ij} is the inter-particle force on particle i due to particle j :

$$F_{ij} = F_{ij}^C + F_{ij}^D + F_{ij}^R \tag{11}$$

3. Results and discussion

In this section, we present results concerning the flow properties such as density, velocity, pressure, and temperature distributions and the effective slip velocity at the rough and the lower flat wall as a function of the

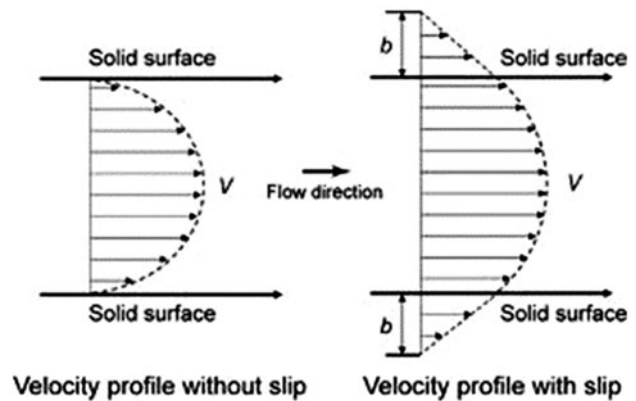


Fig. 2. Velocity profile with slip for flat walls [27].

external driving force, the protrusion height, and length.

Number density profiles at the protrusion and the cavity ($x = \text{const}$) midplanes are presented in Fig. 3. Fluid particle localization is similar for the nanochannel and the microscale channel case as for both cases. three peak density values are detected at the same distance from the upper, the lower, and the protrusion wall surface. The distance differs for the nanochannel and the microchannel case in DPD units ($0.87 r_c$ and $0.44 r_c$, respectively). For the nanochannel at the protrusion, midpoints density is homogeneous and slightly lower from its initial value in the core of the channel, while at the cavity, midpoints is slightly higher on the contrary to the microscale channel. Inside the cavities, high number density regions are detected for both channel scales. The authors also examined the particle trapping inside the cavities by the computation of the residence time and the analysis of particle trajectories, and the results are discussed in detail in Kasiteropoulou et al. [11] (nanochannel) and in Kasiteropoulou et al. [12] (mesoscale channel).

Regarding the density fluctuations close to the solid walls, we must make some comments. For the nanoscale simulations using DPD, these oscillations are realistic. However, as the DPD particles get larger in size (the case of mesoscale simulations), these oscillations close to the wall extend over larger regions than those corresponding to physical layering zones as discussed in [30–32]. There are several methods that have been developed in order to limit such oscillations [30–32]. Thus, the observed oscillations in the mesoscale case have to be seen with some caution. Of course we must mention that if one wants to represent in detail the situation close to the wall, it is crucial to

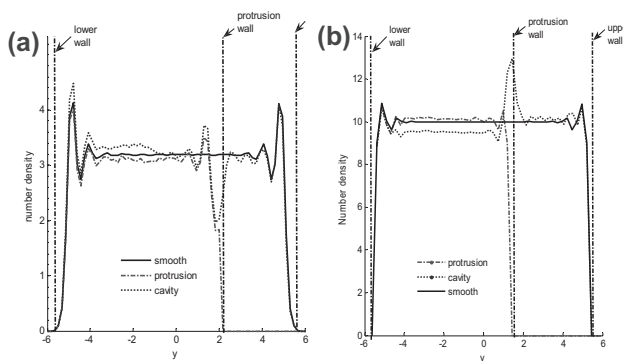


Fig. 3. Local number density profiles at the protrusion midplanes and the cavity midplanes for $F_{\text{ext}} = 0.04$, $l_{r2} = 0.25 l_{\text{tot}}$ and $h = 0.30H$: (a) nanochannel and (b) mesoscale channel (y is in r_c units). Dash-dot lines denote solid wall limits.

implement the above-mentioned methods. However, in our case, we are interested mostly on the qualitative flow behavior as a function of the protrusion height and not to a detailed quantitative study. In a future study, it would be of interest to implement such methods and compare their results as far as the mesoscale is concerned.

The average velocities on layers parallel to the flow are presented in Fig. 4 for a typical nanochannel and microscale channel case. It turns out that the average velocity is systematically reduced as the protrusion height increases for all channel cases investigated in this work.

Pressure behaviour also reveals interesting characteristics (Fig. 5). Both in nanofluidics and microfluidics, pressure remains constant in the central part of the channel and decreases as we move toward to the walls. This reduction is more pronounced as the external driving force increases for all channel cases. High-pressure regions are observed inside the grooves and their magnitude depends on the groove shape (Fig. 5(b1) and (b2)). The average maximum pressure value and the pressure inside the cavities depend both on the protrusion length and height. Smaller protrusion lengths and higher protrusion heights lead in pressure reduction.

Isotherms for typical channel cases are presented in Fig. 6. The temperature field shown in Fig. 5 is presented not as a prediction, but as a pictorial representation of how well the constant temperature assumption is satisfied. In nanofluidics, temperature values in the core of the channel for all grooved channels are lower relative to the initial temperature of the system (see Section 2.2: $T^* = 1$). This reduction depends only on the protrusion length and actually temperature decreases as the protrusion length decreases (Fig. 6(a2)). Keeping the protrusion length constant, the protrusion height does not seem to affect the temperature map. In microfluidics, temperature map reveal differences relative to the nanochannel case. Temperature values in the core of the channel are the same with the initial one independent on the protrusion shape.

The effective slip velocity at the rough wall as a function of the external driving force is presented in Fig. 7 for the nanochannel and in Fig. 8 for the microchannel case. It turns out that the effective slip decreases as the protrusion height increases, whereas for the same protrusion height the effective slip increases as the external driving force increases, both for the nanochannel and the microchannel case.

Moreover, the effective slip decreases as the protrusion length increases (Figs. 9 and 10, respectively)

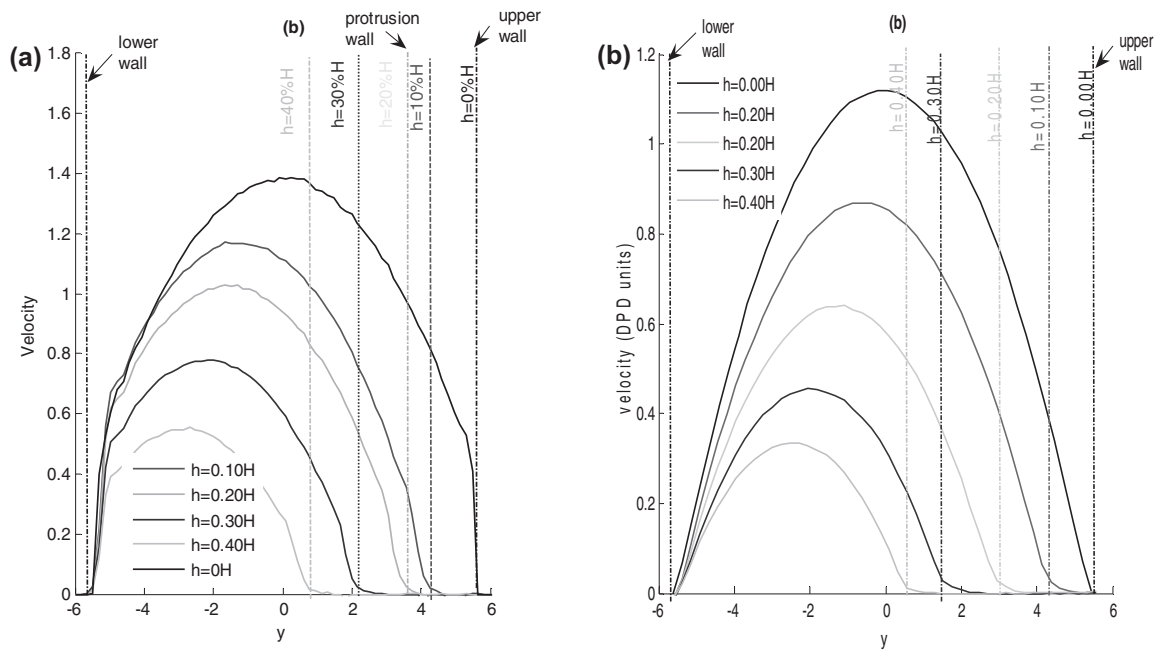


Fig. 4. Bin-averaged velocity profile over the whole channel region for $F_{ext} = 0.02$ and $l_{r2} = 0.25 l_{tot}$: (a) nanochannel and (b) mesoscale channel (y is in r_c units). Dash-dot lines denote solid wall limits.

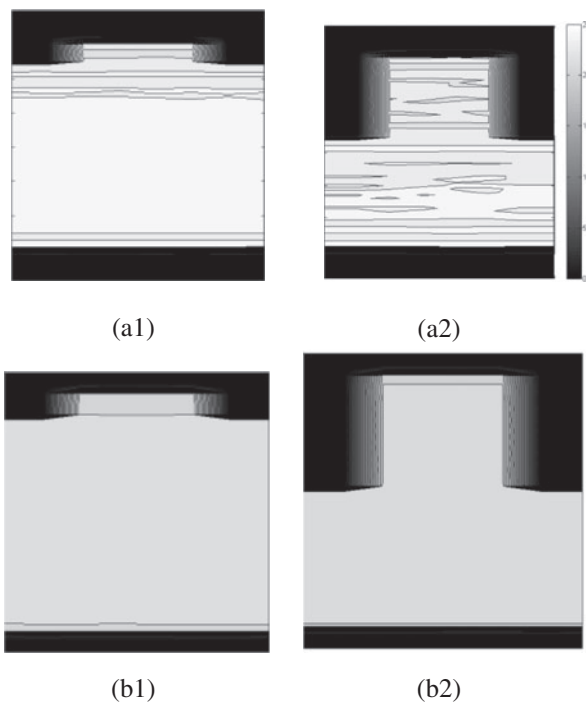


Fig. 5. Isobars of pressure for (a) nanochannel and (b) mesoscale channel for cases (1) $l_{r1} = 0.50 l_{tot}$ and $h = 0.10 H$ and (2) $l_{r1} = 0.50 l_{tot}$ and $h = 0.40 H$. $F_{ext} = 0.02$ DPD units.

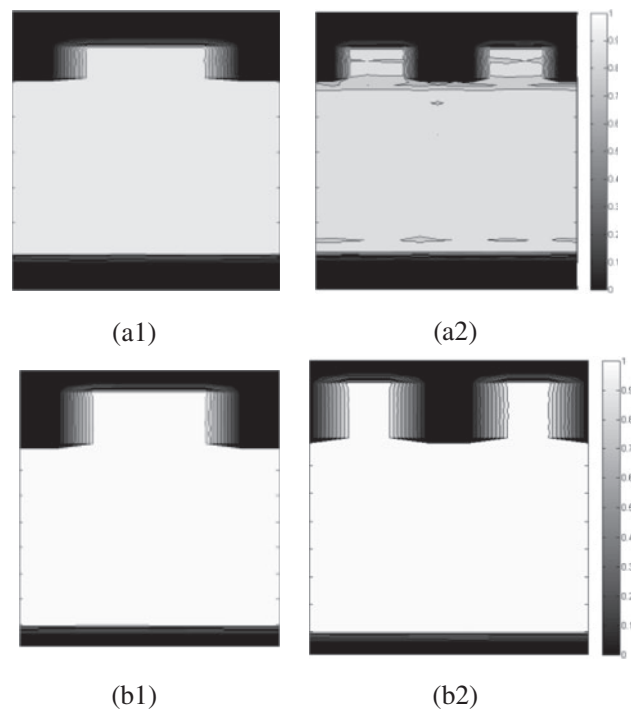


Fig. 6. Isotherms of temperature for (a) nanochannel and (b) mesoscale channel for cases (1) $l_{r1} = 0.50 l_{tot}$ and $h = 0.10 H$ and (2) $l_{r1} = 0.50 l_{tot}$ and $h = 0.40 H$. $F_{ext} = 0.02$ DPD units.

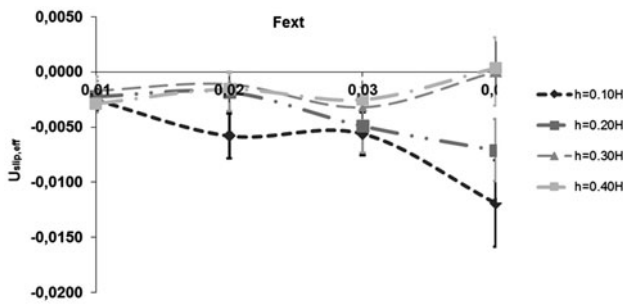


Fig. 7. Estimated velocity slip at the rough wall as a function of external driving force, F_{ext} for the nanochannel. $l_{r2} = 0.25 l_{tot}$ (Curves are just a guide to the eye).

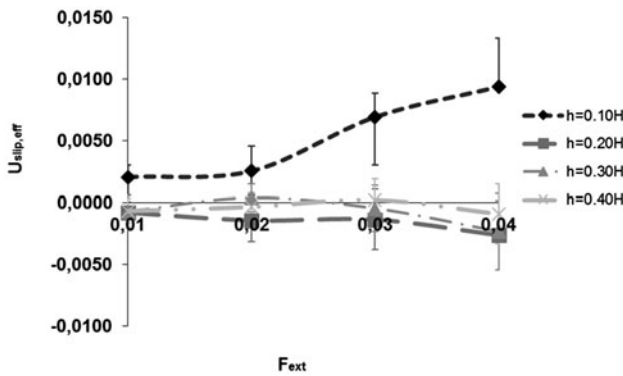


Fig. 8. Estimated velocity slip at the rough wall as a function of external driving force, F_{ext} for the microchannel. $l_{r2} = 0.25 l_{tot}$ (Curves are just a guide to the eye).

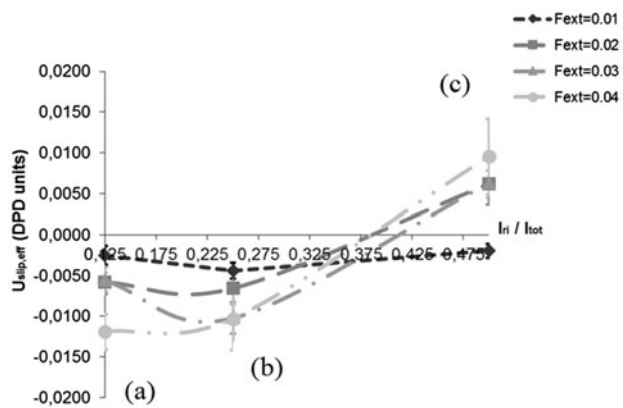


Fig. 9. Estimated velocity slip at the rough wall as a function of protrusion size: (a) $l_{r3} = 0.125 l_{tot}$ (b) $l_{r2} = 0.25 l_{tot}$ and (c) $l_{r1} = 0.50 l_{tot}$ obtained by varying the external driving force, F_{ext} . $h = 0.10 H$. Nanochannel (curves are just a guide to the eye).

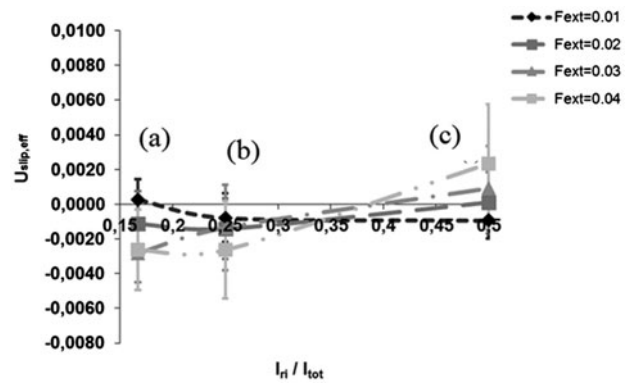


Fig. 10. Estimated velocity slip at the rough wall as a function of protrusion size: (a) $l_{r3} = 0.167 l_{tot}$ (b) $l_{r2} = 0.25 l_{tot}$ and (c) $l_{r1} = 0.50 l_{tot}$ obtained by varying the external driving force, F_{ext} . $h = 0.20 H$. Microchannel (curves are just a guide to the eye).

especially for the higher external driving force investigated in this work ($F_{ext} = 0.04$ DPD units).

The effective slip at the lower flat wall is presented in Fig. 11 (nanochannel) and Fig. 12 (microchannel). It seems that higher slip velocity magnitudes are detected in smaller protrusion heights at the opposite rough walls. In the microscale channel, the velocity slip values are more different as we move toward higher protrusion heights. In particular, in the nanochannel with protrusion length $l_{r3} = 0.125 l_{tot}$, there is a difference in the effective slip for protrusion heights $0.30 H$ and $0.40 H$ equal to 133%, whereas for protrusion length $l_{r3} = 0.167 l_{tot}$ and the same protrusion heights, this difference reaches 25% in the microchannel case; regarding that in the microscale, the lower flat wall is less affected by the upper rough wall.

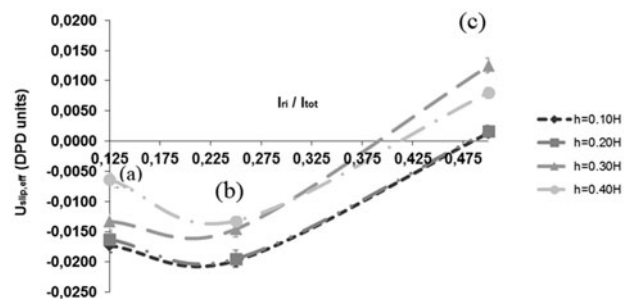


Fig. 11. Estimated velocity slip at the flat wall as a function of the protrusion size placed on the opposite rough wall: (a) $l_{r3} = 0.125 l_{tot}$ (b) $l_{r2} = 0.25 l_{tot}$ and (c) $l_{r1} = 0.50 l_{tot}$ $F_{ext} = 0.01$. Nanochannel (curves are just a guide to the eye).

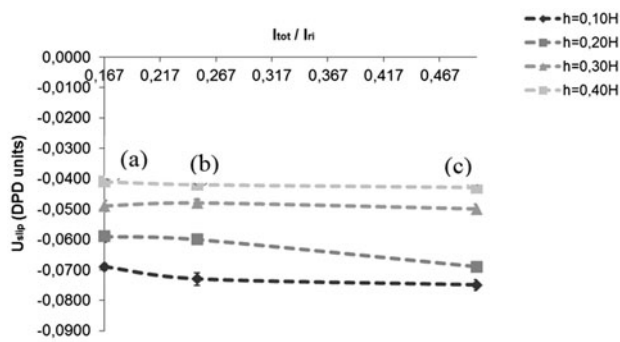


Fig. 12. Estimated velocity slip at the flat wall as a function of the protrusion size placed on the opposite rough wall: (a) $l_{r3} = 0.167 l_{tot}$, (b) $l_{r2} = 0.25 l_{tot}$, and (c) $l_{r1} = 0.50 l_{tot}$, $F_{ext} = 0.02$. Microchannel (curves are just a guide to the eye).

Negative velocities are observed very close to the lower flat wall. Similar behavior is observed in several previous works performed with different simulation methods [33]. For example, Cao [33] studied the surface roughness effect in microscale gas flow by a molecular dynamics simulation and found negative slip for surface roughness equal to 6 nm. Moreover, negative velocities are observed by Guo et al. [34], who studied the slip behavior of dense fluid flows in the nanometer scale using a kinetic model and molecular dynamics simulations.

We must bear in mind that for a flat wall, mesoscale DPD calculations predict a slip at the wall which may be a consequence of imperfect imposition of the boundary conditions as well as an effect of the interactions between the fluid and the solid walls. Consequently, Figs. 11 and 12 describe the deviation expected from the true boundary conditions for the values of the parameters used in the simulations. Given that when we “measure” in the simulations, the velocity of the fluid we calculate in fact an average of the velocities of a limited number of particles close to the wall, the resulting fluctuating velocities that may deviate from the nonslip condition. At the nanoscale case, the interactions between the fluid and the walls may play an important role as well as at very small channel heights, the velocities on the flat wall may be affected by the protrusions that are present on the rough walls. Thus, the results presented should be seen more in a qualitative way.

4. Conclusions

In this paper, we have presented DPD simulations of flow in periodically grooved nano and microchannels. The rough wall was designed by placing a number

of orthogonal protrusions and cavities of equal length. Calculations of the density, velocity, slip velocity, pressure, and temperature show clearly that the presence of protruding elements, the external driving force, and the coarse-graining parameter affect considerably the fluid motion. The presence of the surface periodic protrusions affects clearly the flow close to the wall. The effect of the protruding elements and the driving forces has been also been observed in molecular dynamics simulations (see for example [35,36]).

Inside the cavities, high-density regions and regions of low velocity are observed. When compared to the channel with flat walls, lower flow velocities are observed for all grooved channels and they systematically reduce as the protrusion height increases. Moreover, it turns out that the effective slip on the upper protrusion wall decreases as the protrusion height and the protrusion length increases; whereas for the same protrusion height, the effective slip increases as the external driving force increases, both for the nanochannel and the microchannel case. Negative slip velocities are observed very close to the lower flat walls, in which magnitudes are higher in smaller protrusion heights at the opposite rough walls. Temperature and pressure are homogeneous in the core of the channel and equal to its nominal value.

A comparison between the results of this work and molecular dynamics simulation results has been performed for the slip velocity. They both detected negative slip velocity and they both found higher values for smaller surface roughness values.

The effect of wall roughness on macroscopic quantities is significant and should be further investigated with environmentally friendly materials or different liquid types. One has to take into consideration this effect and envisage the use of such channels for the design of micro and nanofilters useful for environmental applications such as desalination and water purification.

References

- [1] D. Cohen-Tanugi, J.F. Grossman, Water Desalination across Nanoporous Graphene, *Nano Lett.* 12 (2012) 3602–3608.
- [2] T. Humplik, J. Lee, S.C. O’hern, B.A. Fellman, M.A. Baig, S.F. Hassan, M.A. Atieh, Nanostructured materials for water desalination, *Nanotechnology* 22(29) (2011) 292001–292020.
- [3] T. Sochi, Slip at Fluid-Solid Interface, University College London, Department of Physics & Astronomy, London, 2011.
- [4] A. Niavarani, N.V. Priezjev, Modelling the combined effect of surface roughness and shear rate on slip flow of simple fluids, *Phys. Rev. E* 81 (2010) 011606 1–32.

- [5] J. Sun, Y.L. He, W.Q. Tao, J.W. Rose, H.S. Wang, Multi-scale study of liquid flow in micro/nanochannels: Effects of surface wettability and topology, *Microfluid. Nanofluid.* 12 (2012) 991–1008.
- [6] N.V. Priezjev, Interfacial friction between semiflexible polymers and crystalline surfaces, *J. Chem. Phys.* 136 (2012) 224702 1–10.
- [7] W. Chen, R. Zhang, J. Koplik, Velocity slip on curved surfaces, *Condens. Matter*, 1 (2013) 1–5, axix.org/pdf/1309.1423v1.
- [8] I.V. Pivkin, G.E. Karniadakis, A new method to impose no-slip boundary conditions in dissipative particle dynamics, *J. Comput. Phys.* 207 (2005) 114–128.
- [9] A. Kumar, Y. Asako, E. Abu-Nada, M. Krafczyk, M. Faghri, From dissipative particle dynamics scales to physical scales: A coarse-graining study for water flow in microchannel, *Microfluid. Nanofluid.* 7 (2009) 467–477, doi: [10.1007/s10404-008-0398-x](https://doi.org/10.1007/s10404-008-0398-x).
- [10] M. Revenga, I. Zúñiga, P. Español, Boundary conditions in dissipative particle dynamics, *Comput. Phys. Commun.* 121–122 (1999) 309–311, doi: [10.1016/S0010-4655\(99\)00341-0](https://doi.org/10.1016/S0010-4655(99)00341-0).
- [11] D. Kasiteropoulou, T. Karakasidis, A. Liakopoulos, A Dissipative Particle Dynamics study of flow in periodically grooved nanochannels, *Int. J. Numer. Meth. Fl.* 68(9) (2011) 1156–1172.
- [12] D. Kasiteropoulou, T. Karakasidis, A. Liakopoulos, Mesoscopic simulation of fluid flow in periodically grooved microchannels, *Comput. Fluids* 74 (2013) 91–101.
- [13] S.C. Yang, Effects of surface roughness and interface wettability on nanoscale flow in a nanochannel, *Microfluid. Nanofluid.* 2 (2006) 501–511, doi: [10.1007/s10404-006-0096-5](https://doi.org/10.1007/s10404-006-0096-5).
- [14] A. Jabbarzadeh, J.D. Atkinson, R.I. Tanner, Effect of the wall roughness on slip and rheological properties of hexadecane in molecular dynamics simulation of Couette shear flow between two sinusoidal walls, *Phys. Rev. E* 61 (2000) 690–699, doi: [10.1103/PhysRevE.61.690](https://doi.org/10.1103/PhysRevE.61.690).
- [15] G.A. Amhalhel, P. Furmański, Problems of modeling flow and heat transfer in porous media, *J. Power Technol.* 85 (1997) 55–87.
- [16] V.K. Gupta, T.A. Saleh, Sorption of pollutants by porous carbon, carbon nanotubes and fullerene—An overview, *Environ. Sci. Pollut. Res.* 20 (2013) 2828–2843.
- [17] D. Cohen-Tanugi, J.C. Grossman, Water desalination across nanoporous graphene, *Nano Lett.* 12 (2012) 3602–3608.
- [18] J. Lee, T. Laoui, R. Karnik, Nanofluidic transport governed by the liquid/vapour interface, *Nat. Nanotechnol.* 9 (2014) 317–323.
- [19] D.A. Fedosov, I.V. Pivkin, G.E. Karniadakis, Velocity limit in DPD simulations of wall-bounded flows, *J. Comput. Phys.* 227 (2008) 2540–2559, doi: [10.1016/j.jcp.2007.11.009](https://doi.org/10.1016/j.jcp.2007.11.009).
- [20] P. Español, P. Warren, Statistical mechanics of dissipative particle dynamics, *Europhys. Lett. (EPL)* 30 (1995) 191–196. doi: [10.1209/0295-5075/30/4/001](https://doi.org/10.1209/0295-5075/30/4/001).
- [21] R.D. Groot, P.B. Warren, Dissipative particle dynamics: Bridging the gap between atomistic and mesoscopic simulation, *J. Chem. Phys.* 107 (1997) 4423–4435.
- [22] G. Karniadakis, A. Beskok, N. Aluru, *Microflows and Nanoflows: Fundamentals and Simulation*, Springer, New York, NY, 2002.
- [23] Y. Trofimov, Thermodynamic consistency in dissipative particle dynamics, Technische Universiteit Eindhoven, Ph.D. Thesis, 2003.
- [24] S.J. Plimpton, Fast Parallel Algorithms for Short-Range Molecular Dynamics, *J. Comput. Phys.* 117 (1995) 1–19, doi: [10.1006/jcph.1995.1039](https://doi.org/10.1006/jcph.1995.1039).
- [25] G.F. Naterer, P.S. Glockner, D. Thiele, S. Chomokovski, G. Venn, G. Richardson, Surface micro-grooves for near-wall exergy and flow control: Application to aircraft intake de-icing, *J. Micromech. Microeng.* 15 (2005) 501–513, doi: [10.1088/0960-1317/15/3/010](https://doi.org/10.1088/0960-1317/15/3/010).
- [26] D. Kasiteropoulou, T. Karakasidis, A. Liakopoulos, Dissipative Particle Dynamics investigation of parameters affecting planar nanochannel flows, *Mater. Sci. Eng. B* 176(19) (2011) 1574–1579, doi: [10.1016/j.mseb.2011.01.023](https://doi.org/10.1016/j.mseb.2011.01.023).
- [27] A. Liakopoulos, *Fluid Mechanics (in greek)*, Tziolas Publications, Thessaloniki, 2011.
- [28] J.H. Irving, J.G. Kirkwood, The Statistical Mechanical Theory of Transport Processes. IV. The Equations of Hydrodynamics, *J. Chem. Phys.* 18 (1950) 817–830, doi: [10.1063/1.1747782](https://doi.org/10.1063/1.1747782).
- [29] X. Fan, N. Phan-Thien, N. Yong, X. Wu, D. Xu, Microchannel flow of a macromolecular suspension, *Phys. Fluids* 15(1) (2003) 11–21, doi: [10.1063/1.1522750](https://doi.org/10.1063/1.1522750).
- [30] I.V. Pivkin, G. Em. Karniadakis, Controlling density fluctuations in wall-bounded dissipative particle dynamics systems, *Phys. Rev. Lett.* 96 (2006) 206001.
- [31] T. Werder, J.H. Walther, P. Koumoutsakos, Hybrid atomistic–continuum method for the simulation of dense fluid flows, *J. Comput. Phys.* 205 (2005) 373–390.
- [32] Z. Li, Y.-H. Tang, H. Lei, B. Caswell, G. Karniadakis, Energy-conserving dissipative particle dynamics with temperature-dependent properties, *J. Comput. Phys.* 265 (2014) 113–127.
- [33] B.Y. Cao, Non-Maxwell slippage induced by surface roughness for microscale gas flow: A molecular dynamics simulation, *Mol. Phys.* 105(10) (2007) 1403–1410.
- [34] Z. Guo, T.S. Zhao, C. Xu, Y. Shi, Simulation of fluid flows in the nanometer: Kinetic approach and molecular dynamic simulation, *Int. J. Comput. Fluid Dyn.* 20 (6) (2006) 361–367.
- [35] F.D. Sofos, T.E. Karakasidis, A. Liakopoulos, Effects of wall roughness on flow in nanochannels, *Phys. Lett. E* 79 (2009) 026305–1–7.
- [36] F. Sofos, T.E. Karakasidis, A. Liakopoulos, Non-equilibrium molecular dynamics investigation of parameters affecting planar nanochannel flows, *Contemp. Eng. Sci.* 2(6) (2009) 283–298.